A comparison study between the EKF and SIR-PF for GNSS/UWB tight integration

Yihan Guo, Oliviero Vouch, Simone Zocca, Alex Minetto, Fabio Dovis
Department of Electronics and Telecommunications, Politecnico di Torino, Turin, Italy

***Abstract*—The tight integration of Global Navigation Satellite Systems (GNSSs) and low-cost Ultra-Wide Band (UWB) is a prospective positioning solution for autonomous mobile robots that operate in harsh environments with poor satellite visibility. Thanks to the complementarity of the two systems in terms of coverage and ranging performance, the UWB nodes can be used as anchors providing additional ranging measurements. However, the selection of the integration scheme may be a critical issue since high-accuracy positioning performance has to be traded off with the computational complexity of the implementation. This paper compares the performance of two common Bayesian filtering algorithms - the Extended Kalman Filter (EKF) and the Sequential Importance Resampling Particle Filter (SIR-PF) - for the GNSS/UWB tight integration in a dynamic environment. Considering the error sources triggered by the linear approximation employed in the EKF, simulation results show that the performance of the EKF deteriorates more than the SIR-PF when the user's kinematics changes rapidly and when the user gets close to the UWB anchor. Compared to the EKF, the SIR-PF can therefore guarantee superior positioning accuracy even if at the cost of higher computational complexity.**

***Index Terms*—Global Navigation Satellite System, Ultra-Wide Band, Extended Kalman Filter, Particle Filter.**

I. Introduction

AUTONOMOUS mobile robots highly rely on accurate and robust positioning solutions for their navigation and control loops [1]. On the one hand, Global Navigation Satellite System (GNSS) can provide positioning solutions in absolute reference frames. On the other hand, Ultra-Wide Band (UWB) can achieve centimeter-level accurate ranging over short distances [2]. Hence, the integration of GNSS and UWB is growing popularity as a solution for autonomous mobile robots to overcome the GNSS performance degradation due to multipath and signal blockages [3].

GNSS/UWB integrated systems generally leverage Bayesian formulations of maximum-a-posteriori state estimation [4]. As a matter of fact, GNSS and UWB measurement functions are inherently non-linear; it follows their first-order Taylor approximation in the Extended Kalman Filter (EKF) state-space formulation [5]. Alternatively, sequential Monte-Carlo (MC) methods such as the Sequential Importance Resampling Particle Filter (SIR-PF) can directly handle state-estimation over non-linear and non-Gaussian state-space distributions [6]. However, besides avoiding linearizations, these algorithms come at the cost of increased computational loads, and techniques have been proposed in literature to mitigate this [7]. Overall, for a specific application, the filter selection should be determined based on whether the accuracy gain is worth the extra computational cost.

Two scenarios are typically considered when addressing the integration of GNSS and UWB sensors; on the one hand, UWB anchors can be deployed in fixed and geo-referenced locations [8], [9]. Alternatively, UWB transceivers can be installed on moving platforms such as Unmanned Aerial Vehicles (UAVs) [10]. Both approaches aim at exploiting the high-accuracy ranging potential of UWB, although a limited coverage can be afforded by this technology. In the case of mobile platforms, however, uncertainties in the determination of the locations of UWB anchors can induce extra errors in the estimated position of the receiver.

Focusing on GNSS/UWB tight integration, this paper aims at comparing the performance based on the EKF and PF schemes in the specific scenario in which the GNSS measurements are integrated with ranging measurements from UWB mobile sensors locally deployed. In this scenario, it is theoretically shown how the linearization process embedded in the EKF introduces approximation errors, while the PF architecture is more effective. Besides, the specific factors in the GNSS/UWB tight integration causing EKF approximation errors are analyzed and concluded. The simulation compares the positioning accuracy and computational loads for both filtering architectures, providing guidelines for the design of a suitable integration scheme.

II. Background

In this Section, the Bayesian recursive formulations of both the EKF and the Sequential Importance Resampling Particle Filter (SIR-PF) are briefly reviewed [11].

A. Extended Kalman Filter

The EKF undertakes a discrete, linear and Gaussian state-space approximation, and it pursues Position, Velocity, Timing (PVT) estimation in two steps:

a) Prediction step:

$$\hat{\boldsymbol{x}}_k^- = \boldsymbol{f}(\hat{\boldsymbol{x}}_{k-1}) \tag{1}$$

$$\hat{\boldsymbol{P}}_k^- = \boldsymbol{A}_k \hat{\boldsymbol{P}}_{k-1} \boldsymbol{A}_k^T + \boldsymbol{Q}_k \tag{2}$$

b) Update step:

$$\boldsymbol{K}_k = \hat{\boldsymbol{P}}_k^- \boldsymbol{H}_k^T (\boldsymbol{H}_k \hat{\boldsymbol{P}}_k^- \boldsymbol{H}_k^T + \boldsymbol{R}_k)^{-1} \tag{3}$$

$$\hat{\boldsymbol{x}}_k = \hat{\boldsymbol{x}}_k^- + \boldsymbol{K}_k(\boldsymbol{y}_k - \boldsymbol{h}(\hat{\boldsymbol{x}}_k^-)) \tag{4}$$

$$\hat{\boldsymbol{P}}_k = (\boldsymbol{I} - \boldsymbol{K}_k \boldsymbol{H}_k)\hat{\boldsymbol{P}}_k^- \tag{5}$$

where:

- $\hat{\boldsymbol{x}}_k^-$ is the prior state estimate at epoch k;
- $\hat{\boldsymbol{x}}_k$ is the posterior state estimate at epoch k;
- $\boldsymbol{f}(\cdot)$ is a set of state transition functions;
- $\boldsymbol{A}_k$ is the Jacobian matrix of the state transition function w.r.t. the state vector $\boldsymbol{x}_k$
- $\boldsymbol{H}_k$ is the Jacobian matrix of the measurement function w.r.t. the state vector $\boldsymbol{x}_k$
- $\hat{\boldsymbol{P}}_k^-$ is the prior estimate of the state covariance matrix at epoch k;
- $\hat{\boldsymbol{P}}_k$ is the posterior estimate of the state covariance matrix at epoch k;
- $\boldsymbol{y}_k$ is the vector of measurements at epoch k;
- $\boldsymbol{h}(\cdot)$ is a set of measurement functions;
- $\boldsymbol{K}_k$ is the Kalman gain matrix at epoch k;
- $\boldsymbol{I}$ the identity matrix.

B. Sequential Importance Resampling Particle Filter

In the family of sequential MC methods, the SIR-PF can directly handle non-linear, non-Gaussian state-space representations. The SIR-PF algorithm is summarized as follows:

- **Initialization**: Sample N particles $\boldsymbol{x}_0^{(i)}$ from the prior state distribution $p(\boldsymbol{x}_0)$ and assign them equal weights $w_0^{(i)}$:

$$\begin{aligned} &\boldsymbol{x}_0^{(i)} \sim p(\boldsymbol{x}_0) \\ &w_0^{(i)} = 1/N,\ i = 1, ..., N \end{aligned} \tag{6}$$

- **Recursive estimation**: For every filtering epoch, the following steps are operated:
  1) Sample particles from the importance distribution:

$$\boldsymbol{x}_k^{(i)} \sim p(\boldsymbol{x}_k \mid \boldsymbol{x}_{k-1}),\ i = 1, ..., N \tag{7}$$

  which is set as the transition probability distribution $p(\boldsymbol{x}_k \mid \boldsymbol{x}_{k-1})$ [11].
  2) Update particle weights:

$$w_k^{(i)} \propto w_{k-1}^{(i)} p(\boldsymbol{y}_k \mid \boldsymbol{x}_k^{(i)}) \tag{8}$$

  where $p(\boldsymbol{y}_k \mid \boldsymbol{x}_k^{(i)})$ is the conditional probability distribution of the measurements given the i-th particle realization $\boldsymbol{x}_k^{(i)}$. Weights $\{w_k^{(i)}\}_{i=1}^N$ are normalized and sum to unity.
  3) Compute the effective number of particles [11]:

$$N_{eff} = \left(\sum_{i=1}^{N} \left(w_k^{(i)} \right)^2 \right)^{-1} \tag{9}$$

  and compare the N_{eff} with a predefined threshold N_{th} to decide whether or not to execute resampling.

III. Methodology

The detailed state transition and measurement functions of the state-space model for GNSS/UWB tight integration can be found in [12]. The PF is not able to leverage the motion model consisting of acceleration since there are no measurements in both GNSS and UWB reflecting acceleration. To make a fair comparison, the state transition model only contains the states of position, velocity, receiver clock bias, and drift. Tailored to this framework, the choice of using either the EKF or the SIR-PF consists in making a trade-off between the positioning performance and the computational burden.

In order to decide which is the most profitable way to implement the integration, it is worth investigating the factors impacting the EKF accuracy performance and the specific degree of accuracy deterioration. As it is known, the Kalman Filter (KF) has been proven as the optimal filter for linear state-space models and Gaussian noises [11]. In the prediction step, both the EKF and SIR-PF use the same discretization strategy to model the dynamics of the user, which results in the same level of prediction errors. For the update step, instead, the SIR-PF can precisely approximate the non-linear measurement functions with increasing particle numbers using the Monte Carlo method. On the other hand, the EKF linearization of the measurement function brings about approximation errors. These errors are caused by the omission of terms in the Taylor expansion, which is shown as follows:

$$\begin{aligned} y_{k,j} = {} & h(\hat{\boldsymbol{x}}_k^-) + \boldsymbol{H}_{k,j}(\boldsymbol{x}_k - \hat{\boldsymbol{x}}_k^-) + \frac{1}{2}(\boldsymbol{x}_k - \hat{\boldsymbol{x}}_k^-)^T \boldsymbol{B}_{k,j}(\boldsymbol{x}_k - \hat{\boldsymbol{x}}_k^-) \\ & + O_j(\boldsymbol{x}_k - \hat{\boldsymbol{x}}_k^-) + w_{k,j} \end{aligned} \tag{10}$$

where $y_{k,j}$ is the j-th scalar component of the measurement vector $\boldsymbol{y}_k$, $\boldsymbol{H}_{k,j}$ and $\boldsymbol{B}_{k,j}$ are the Jacobian and Hessian matrices of the j-th measurement function w.r.t. the state vector $\boldsymbol{x}_k$. $O_j(\boldsymbol{x}_k - \hat{\boldsymbol{x}}_k^-)$ lumps all the items in the Taylor expansions whose orders are higher than two and $w_{k,j}$ is the measurement noise for the j-th measurement at epoch k.

The approximation error is the sum of all the terms whose order is higher than one since the EKF only employs the first-order term of the Taylor expansion. Due to the component of the factorial's reciprocal, high-order terms are increasingly smaller in quantity w.r.t. the second-order term, so they can be neglected to simplify the analysis.

Hence, the decomposition of the second-order term reveals the error sources, listed as:

- $\boldsymbol{x}_k - \hat{\boldsymbol{x}}_k^-$ is the difference between the prior and true states, which is called the prediction error;
- $\boldsymbol{B}_k$ is the Hessian matrix, which is related to the measurement function at the linearization point.

Based on the state transition function for GNSS/UWB tight integration, the prediction error depends on two factors which are the dynamic motion of the user and the time interval between measurements. Higher dynamics, i.e., higher changing rate for velocity and position, means larger prediction errors. Similarly, the longer the time interval of measurements, the lower the prediction accuracy will be.

The second component is the Hessian matrix, which collects the second-order partial derivatives of the non-linear measurement function about the linearization point. For the GNSS/UWB tight integration, non-linear measurement functions involve both the GNSS pseudorange function and the UWB ranging function, which are both spherical functions. Regarding GNSS, the position of the satellite is the sphere center, while the measured pseudorange is the radius. Similarly, for UWB the position of the UWB tag is the center and the ranging measurement of the UWB transceiver is the radius. Implementing a linear approximation using the Taylor expansion to a spherical function, the result will be a plane tangent to the sphere at the linearization point. Therefore, in a given neighborhood of the linearization point, a small radius results in a large curvature, consequently leading to large approximation errors. The Hessian matrix reflects this kind of approximation errors. In this research, the UWB spherical measurement function's radius is much smaller than that of GNSS, so the UWB linearization error is larger than that of GNSS.

IV. Results

This section presents simulation results to compare the performances between the EKF and the SIR-PF for GNSS/UWB tight integration, analyzing approximation errors.

A. Simulation set-up

The simulated environment is generated from a Radio Frequency GNSS simulator – IFEN Network Constellation Simulator (NCS) Titan. All the GNSS measurements (pseudorange and Doppler-shift) are from GPS L1 C/A signals collected at a frequency of $10\,\mathrm{Hz}$. To focus on the impact of the filter selection on the positioning performance, the simulated GNSS pseudorange measurements are only impaired by receiver noise, but free from all other error sources such as atmospheric delays, ephemeris errors, etc. The receiver noise follows a Gaussian distribution with zero mean and $1\,\mathrm{m}$ standard deviation. The GNSS simulator provides the ground truth so the positioning error can be computed. The ground truth is a Bernoulli Lemniscate trajectory, as shown in Fig. 4.

To investigate the impact of the approximation error in the EKF due to UWB measurements, only one UWB anchor is deployed. This anchor is placed $20\,\mathrm{m}$ away from the center of the trajectory, with a height of $5\,\mathrm{m}$. UWB measurements are synthetically generated following the model from [13]. In addition, UWB and GNSS measurements are accurately synchronized and processed at $10\,\mathrm{Hz}$ rate.

Given the aforementioned set-up, two trajectories are simulated at different average receiver speeds of $2\,\mathrm{m/s}$ and $10\,\mathrm{m/s}$, respectively.

For both the EKF and the SIR-PF, the details about the process noise covariance parametrization can be found in [12]. As regards measurement noise covariance statistics in $\boldsymbol{R}_k$, the model proposed in [14] is leveraged for GNSS. While the standard deviation of the UWB measurement noise is set as $0.05\,\mathrm{m}$ based on the model from [13]. Furthermore, the number of particles is set to 10^4 for the SIR-PF, and N_{th} is set to 0.5. The experimental results of the SIR-PF are based on 20 Monte Carlo simulations.

B. Analysis of EKF approximation errors

Given the analysis in Section III, it was determined that the prediction error is larger with an increase in dynamics. Therefore, the aim of the experiment is to test this by comparing positioning results from two datasets with different vehicle velocities: $2\,\mathrm{m/s}$ and $10\,\mathrm{m/s}$. The positioning errors under a local East North Up (ENU) coordinate system are shown in Fig. 1. It can be seen that the positioning errors of EKF and the SIR-PF are pretty similar in the dataset with $2\,\mathrm{m/s}$ of user velocity, while the performance gap in favor of the SIR-PF is larger for the dataset with $10\,\mathrm{m/s}$. In the latter scenario, the positioning error contains several spikes, which are marked with their exact values in the plots. Fig. 2 gives the Cumulative Density Function (CDF) curves of positioning errors for both filters under different user velocities. Table I summarizes the whole trajectory positioning Root-Mean-Square Error (RMSE)s for the two architectures in each experiment. All the results show that the accuracy deterioration of the SIR-PF is much smaller compared to that of EKF when the dynamics increase. For the sake of completeness, we also provide a comparison of computational loads, the EKF and the SIR-PF take $1.6907\,\mathrm{s}$ (946 epochs per second) and $7.4827\,\mathrm{s}$ (213 epochs per second) for the entire trajectory (1600 epochs), respectively, based on the aforementioned simulation settings.

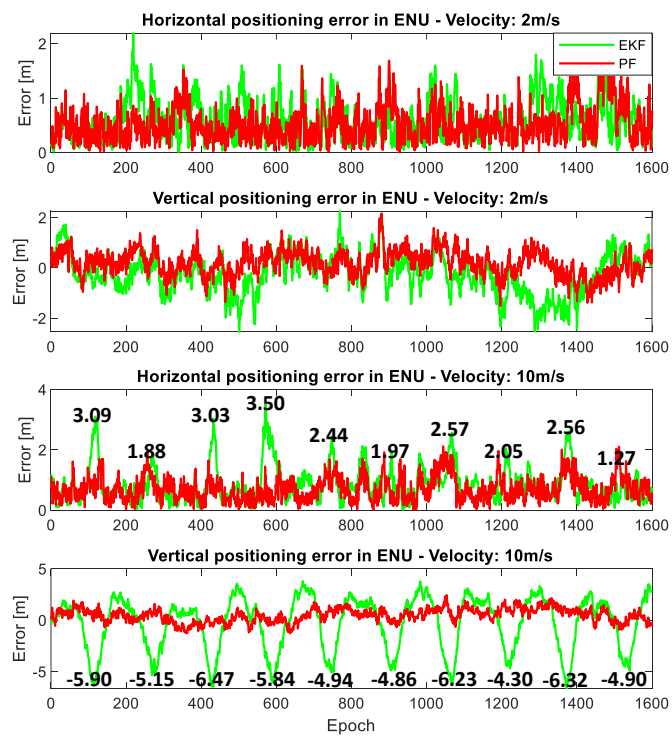

Fig. 1: Horizontal and vertical positioning error for the EKF and the SIR-PF architectures shown for different vehicle velocities.

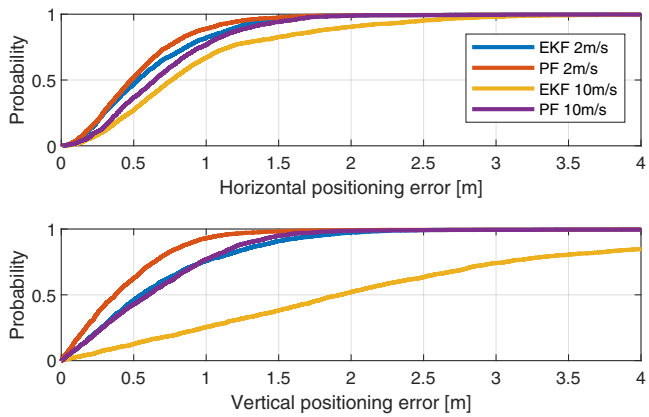

Fig. 2: Horizontal and vertical positioning CDFs for the EKF and the SIR-PF architectures shown for different vehicle velocities.

Several error spikes appear periodically in both horizontal and vertical directions in Fig. 1. To analyze the relationship between these spikes and the prediction errors, the data from one period of the trajectory are isolated. Then, Fig. 3 shows the time series of the Euclidean norms of prediction errors, as well as accelerations from the ground truth, and aligns them with the positioning errors over time. Unmodeled accelerations can be viewed as noises in the state transition function and lead to prediction errors. Based on the discussion in Section III, prediction errors further amplify approximation errors for the EKF. In other words, linearization of a sphere function causes an error proportional to the second-term of the Taylor expansion, and the linearization point for the EKF is based on the predicted state, which in turn also suffers from errors due to discretization of user dynamics, thus further amplifying the linearization error. Since the SIR-PF does not perform linearization, it suffers less impact from the prediction error. This explains well why the peaks in acceleration values match the maximum prediction and positioning errors.

Furthermore, Fig. 4 depicts the whole trajectory in one period with the corresponding prediction error value of every point. The leftmost and rightmost endpoints of the trajectory have the largest accelerations of the vehicle's dynamic, matching the two error peaks.

C. Analysis of EKF errors due to the Hessian matrix

Based on the analysis in Section III, the Hessian matrix is also a component of the second-order term besides the prediction error. However, the physical meaning of the Euclidean norm of a matrix is not as obvious as it for a vector. With the aim of interpreting the results, this experiment focuses more on the effect of the Hessian matrix on the linear transformation in the second-order term of the Taylor expansion. As it happens, the prediction errors are the same for all different measurements under one epoch. Therefore, the values of the second-order terms $\frac{1}{2}(\boldsymbol{x}_k - \hat{\boldsymbol{x}}_k^-)^T \boldsymbol{B}_{k,j}(\boldsymbol{x}_k - \hat{\boldsymbol{x}}_k^-)$ are only influenced by their Hessian matrices, which reflects the geometry for GNSS and UWB. This provides us with a fair and easy way to monitor the influence of Hessian matrices, which is to compare the values of second-order terms from different measurement functions under a given epoch.

Fig. 5 shows all the second-order terms in the Taylor expansion for every GNSS satellite in one period of the trajectory. First-order terms are provided as a reference. All the second-order terms of GNSS are negligible if compared to the

TABLE I: Positioning RMSEs for the EKF and the SIR-PF under different vehicle velocities for the whole trajectory.

Vehicle velocity	Filter type	RMSE [m]	
		Horizontal	Vertical
2 m/s	EKF	0.6881	0.8384
	SIR-PF	0.6187	0.5486
10 m/s	EKF	1.0248	2.6060
	SIR-PF	0.7652	0.8084

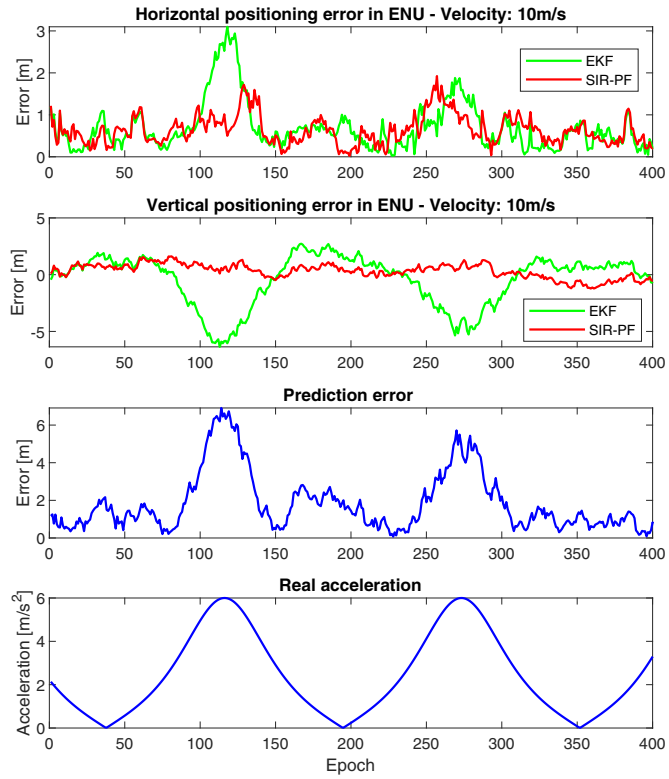

Fig. 3: Horizontal and vertical position and prediction errors for the EKF and the SIR-PF architectures.

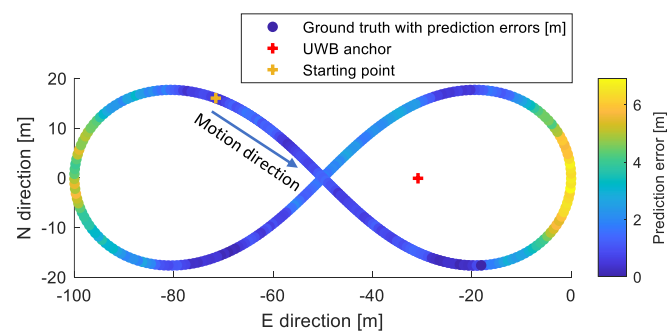

Fig. 4: Vehicles trajectory and location of the UWB anchor. The prediction error along the path follows the colorscale.

first-order terms. The latter shows that linear approximation is more accurate for GNSS measurements. However, UWB measurements perform differently as depicted by Fig. 6. The value of second-order terms is much larger for UWB measurements, thus indicating that approximation errors are much higher w.r.t. GNSS measurements. In addition, two spikes are found with different magnitudes in the second-order terms. From the result of the previous subsection, it is known that the prediction errors of these two spikes are closely related to the acceleration, which means that the peak's value of the spike is only determined by the Hessian matrix. Moreover, the larger spike corresponds to the vehicle's location being closest to the UWB anchor. This experimentally validates the assumptions in Section III that a smaller radius of UWB ranging leads to a larger linear approximation error.

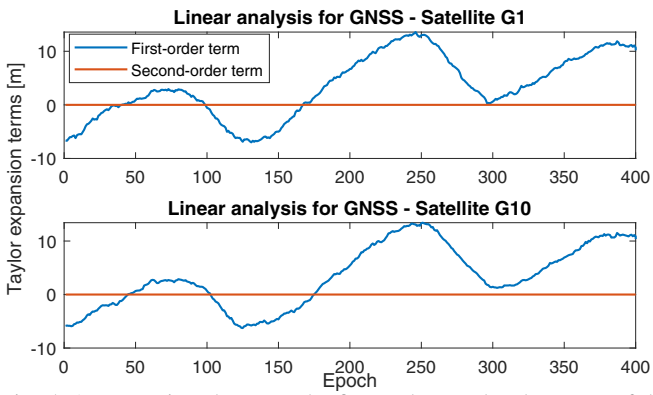

Fig. 5: A comparison between the first and second-order terms of the Taylor expansion for GNSS pseudorange measurements.

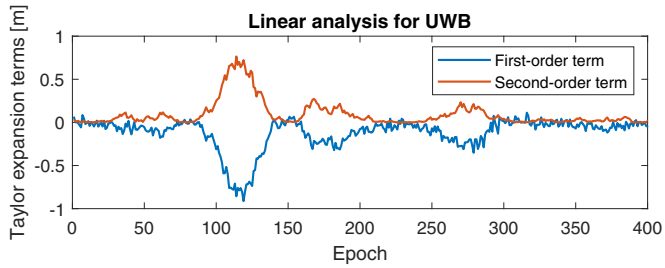

Fig. 6: A comparison between the first and second-order terms of the Taylor expansion for UWB range measurements

V. Conclusions

For the GNSS/UWB tight integration, this paper analyzes and compares two classical Bayesian filters – the EKF and the SIR-PF. From the Taylor expansion utilized in the EKF, the approximation error sources are determined as the prediction error and the Hessian matrix of measurement functions w.r.t. states. For the specific integration scheme as the UWB/GNSS tight integration, this research concludes that the prediction error is caused by the sampling interval of measurements and the user's dynamic. Meanwhile, the Hessian matrix is determined by the distance from the UWB anchor to the user. According to the above factors causing approximation errors, simulated experiments are designed. Experimental results demonstrate that EKF produces large positioning errors in high-dynamic scenarios and when the user is closer to the UWB anchors. On the contrary, the SIR-PF performs much better under the above conditions. The results of this paper provide a reference to select a suitable integration scheme for GNSS/UWB integration depending on the scenario.

VI. Acknowledgment

This work has been supported by the Politecnico di Torino Interdepartmental Centre for Service Robotics PIC4SeR. Y. Guo acknowledges the Chinese Scholarship Council (CSC). A. Minetto acknowledges funding from the research contract no. 32-G-13427-5 DM 1062/2021 funded within the Programma Operativo Nazionale (PON) Ricerca ed Innovazione of the Italian Ministry of University and Research (MUR).

References

[1] S. Kuutti, S. Fallah, K. Katsaros, M. Dianati, F. McCullough, and A. Mouzakitis, "A survey of the state-of-the-art localization techniques and their potentials for autonomous vehicle applications," *IEEE Internet of Things Journal*, vol. 5, no. 2, pp. 829–846, 2018.

[2] R. Zekavat and R. M. Buehrer, "Wireless Localization Using Ultra-Wideband Signals," in *Handbook of Position Location: Theory, Practice, and Advances*. Wiley-IEEE Press, 2019, pp. 269–301.

[3] E. Kaplan, J. Leva, D. Milbert, and M. Pavloff, "Fundamentals of Satellite Navigation," in *Understanding GPS: Principles and Applications*, 2nd ed. Artech House, 2017, ch. 2, pp. 21–63.

[4] G. M. Hoang, B. Denis, J. Härri, and D. Slock, "Bayesian fusion of GNSS, ITS-G5 and IR–UWB data for robust cooperative vehicular localization," *Comptes Rendus Physique*, vol. 20, no. 3, pp. 218–227, 2019.

[5] M. I. Ribeiro, "Kalman and extended Kalman filters: Concept, derivation and properties," *Institute for Systems and Robotics*, vol. 43, p. 46, 2004.

[6] F. Gustafsson, F. Gunnarsson, N. Bergman, U. Forssell, J. Jansson, R. Karlsson, and P.-J. Nordlund, "Particle filters for positioning, navigation, and tracking," *IEEE Transactions on signal processing*, vol. 50, no. 2, pp. 425–437, 2002.

[7] S. Zocca, Y. Guo, A. Minetto, and F. Dovis, "Improved weighting in particle filters applied to precise state estimation in GNSS," *Frontiers in Robotics and AI*, vol. 9, p. 950427, 2022.

[8] B. Zhu, X. Tao, J. Zhao, M. Ke, H. Wang, and W. Deng, "An integrated GNSS/UWB/DR/VMM positioning strategy for intelligent vehicles," *IEEE Transactions on Vehicular Technology*, vol. 69, no. 10, pp. 10 842–10 853, 2020.

[9] W. Jiang, Z. Cao, B. Cai, B. Li, and J. Wang, "Indoor and outdoor seamless positioning method using UWB enhanced multi-sensor tightly-coupled integration," *IEEE Transactions on Vehicular Technology*, vol. 70, no. 10, pp. 10 633–10 645, 2021.

[10] O. Vouch, Y. Guo, S. Zocca, A. Minetto, and F. Dovis, "Improved Outdoor Target Tracking via EKF-based GNSS/UWB Tight Integration with Online Time Synchronisation," in *Proceedings of the 35th International Technical Meeting of the Satellite Division of The Institute of Navigation (ION GNSS+ 2022)*, Sep. 2022, pp. 2409–2422, iSSN: 2331-5954.

[11] S. Särkkä, *Bayesian filtering and smoothing*. Cambridge university press, 2013, no. 3.

[12] Y. Guo, O. Vouch, S. Zocca, A. Minetto, and F. Dovis, "Enhanced EKF-based time calibration for GNSS/UWB tight integration," *IEEE Sensors Journal*, vol. 23, no. 1, pp. 552–566, 2022.

[13] A. De Preter, G. Goysens, J. Anthonis, J. Swevers, and G. Pipeleers, "Range bias modeling and autocalibration of an uwb positioning system," in *2019 International Conference on Indoor Positioning and Indoor Navigation (IPIN)*. IEEE, 2019, pp. 1–8.

[14] H. Kuusniemi, A. Wieser, G. Lachapelle, and J. Takala, "User-level reliability monitoring in urban personal satellite-navigation," *IEEE Transactions on Aerospace and Electronic Systems*, vol. 43, no. 4, pp. 1305–1318, 2007.